ACS APPLIED NANO MATERIALS

Article

Characterization of Nanomaterials by Locally Determining their Complex Permittivity with Scattering-Type Scanning Near Field Optical Microscopy

Stefan G. Stanciu, Denis E. Tranca, Laura Pastorino, Stefania Boi, Young Min Song, Young Jin Yoo, Satoshi Ishii, Radu Hristu, Fang Yang, Gianlorenzo Bussetti, and George A. Stanciu

ACS Appl. Nano Mater., **Just Accepted Manuscript** • DOI: 10.1021/acsanm.9b02019 • Publication Date (Web): 10 Jan 2020

Characterization of Nanomaterials by Locally Determining their Complex Permittivity with Scattering-Type Scanning Near Field Optical Microscopy

Stefan G. Stanciu[1*], Denis E. Tranca[1], Laura Pastorino[2*], Stefania Boi[2], Young Min Song[3*], Young Jin Yoo[3], Satoshi Ishii[4*], Radu Hristu[1], Fang Yang[5], Gianlorenzo Bussetti[6], George A. Stanciu[1]

1) Center for Microscopy-Microanalysis and Information Processing, Politehnica University of Bucharest, Bucharest 060424, Romania
2) Department of Informatics, Bioengineering, Robotics and Systems Engineering, University of Genoa, Genoa, Italy
3) Gwangju Institute of Science and Technology, Gwangju, South Korea
4) International Center for Materials Nanoarchitectonics, National Institute for Materials Science, Tsukuba, Japan
5) Cixi Institute of Biomedical Engineering, CAS Key Laboratory of Magnetic Materials and Devices & Key Laboratory of Additive Manufacturing Materials of Zhejiang Province, Ningbo Institute of Materials Technology and Engineering, Chinese Academy of Sciences, Ningbo 315201, P.R. China
6) Department of Physics, Politecnico di Milano, Milan, Italy

Corresponding authors:

stefan.stanciu@cmmip-upb.org

laura.pastorino@unige.it

ymsong@gist.ac.kr

sishii@nims.go.jp

Abstract:

Scattering-type Scanning Near Field Optical Microscopy (s-SNOM) is currently regarded as a powerful tool for exploring important optical properties at nanoscale resolutions depending only on the size of a sharp tip that is scanned across the sample surface while being excited with a focused laser beam. Recently, it was shown that, among others, s-SNOM can quantitatively map the complex permittivity of materials and biological samples, and hence other intrinsic related optical properties, such as the refractive index. In this work we apply this capability, previously demonstrated only at proof-of-concept level, in an experiment dealing with three distinct types of nanostructured materials: microcapsules for drug delivery assembled with layer-by-layer strategies, ultra-thin optical coatings with tunable color properties, and plasmonic ceramic nanoparticles. We show that complex permittivity mapping with s-SNOM can contribute to the better understanding of such materials, providing information which is difficult or even impossible to assess with other techniques.

Keywords: scattering-type scanning near-field optical microscopy, nanoscale imaging, complex permittivity, layer-by-layer microcapsules, ultra-thin optical coatings, ceramic nanoparticles.

1. Introduction

Understanding in depth the fundamental properties of biological samples and advanced materials requires their thorough characterization at micro- and nanoscales, the latter being obviously more difficult to investigate. This has motivated the scientific communities working in optics and photonics to place massive efforts over the past years in the quest for developing novel imaging techniques capable of optical resolutions surpassing the diffraction limit. Although their advent immediately generated huge impact in life sciences, fluorescence based Super-Resolution Microscopy (SRM) modalities[1] that offer typical resolutions in the range of 20-100 nm face a series of limitations due to the lack of chemical sensitivity and dependence on fluorescent probes, which restricts their use to a limited range of samples, mainly of biological origin. Such limitations and concerns keep scientists motivated to innovate alternative ways of overcoming the diffraction barrier, in the form of optical imaging techniques that do not require contrast agents, ("label-free"). Among the label-free optical nanoscopy techniques that have emerged over the past years, two prominent families can be easily distinguished: (a) nanoscopy techniques based on the interaction of light and a sharp tip scanned across the sample surface, such as scattering-type Scanning Near-Field Optical microscopy (s-SNOM)[2], tip-enhanced Fluorescence (TEF)[3], tip-enhanced Raman Spectroscopy (TERS)[4], Photoinduced Force Microscopy (pi-FM) [5], or Photothermal Atomic Force Microscopy (photothermal-AFM)[6], and b) far-field techniques based on pump and probe strategies where two or more incident beams compete, such as Saturated Transient Absorption Microscopy [7-8], Super-Resolution Photomodulated Reflectivity[9] or Saturated Stimulated-Raman-Scattering[10]. All these "label-free" techniques hold significant potential for the nanoscale characterization of advanced materials as a result of not requiring labeling and allowing thus an unbiased characterization of a specimen's intrinsic physico-chemical properties.

In this article we focus our attention on s-SNOM, a generally applicable label-free method for surface characterizations at nanoscale resolution[2], whose working principles rely on a sharp tip that is scanned across the sample while being excited with a focused laser beam, converting the illumination radiation into a highly localized and enhanced near-field at the tip apex. The optical interaction between this enhanced near-field and the sample volume underneath modifies both the amplitude and the phase of the scattered excitation light, depending on the local dielectric properties of the sample[11]. Interferometric detection of the backscattered light yields nanoscale-resolved amplitude and phase images, that can reveal various important properties of nanostructured materials[2]. The wide availability of light sources that can be used in association with s-SNOM, performing in continuous, high-repetition-rate or low-repetition-rate modes[12], and frequencies ranging from visible light to terahertz[13-15], proposes s-SNOM to become a standard for high-spatial-resolution surface analysis. Its complex but reliable contrast mechanism enabled so far a wide range of discoveries in the condensed phase materials, and two-dimensional materials[16-22].

With respect to imaging biological species, a limited number of experiments have been performed so far with s-SNOM but these demonstrate nonetheless its potential in this regard[23-26]. s-SNOM has also been fruitfully employed in various correlative imaging approaches such as the correlation of the infrared optical contrast with the structural state of a phase changing material[27], establishing the relation between conductivity and crystal structure in ZnO nanowire cross-sections[28], mapping of surface charge domains[29] or correlative nanoimaging of areas with strongly enhanced electromagnetic fields and Raman scattering[30]. These previous experiments demonstrate s-SNOM's potential to complement other nano- or micro-scale techniques, which is of great benefit with respect to a better understanding of advanced materials.

In recent proof-of-concept experiments it was shown that s-SNOM data can be processed to determine the real and imaginary parts of the dielectric function, and hence of optical parameters such as refractive index, transmittance, reflectance, absorption, etc. [31-32]. In this work we exploit these capabilities in a set of precise applications focused on three distinct types of advanced nanostructured materials: (i) microcapsules for drug delivery assembled with layer-by-layer strategies [33-34], (ii) ultra-thin optical coatings with tunable color properties [35], and (iii) ceramic plasmonic nanoparticles[36-37]. The scientific relevance of these three different types of nanostructured samples, will be briefly discussed in the next paragraphs.

Polyelectrolyte multilayered capsules (PMCs): The development of micro- and nano-sized systems that can be functionalized to carry bioactive substances at specific sites within the human body and to release these at controlled time intervals, or under specific external or internal stimuli, is of great interest at the time being. Among these, PMCs have been widely studied as prominent candidates for the delivery of bioactive molecules[38],[39]. This is because the properties of the shell layers, and also of the cores, can be tailored in order for the capsules to react in specific ways under diverse internal or external stimuli, such as various proteins or antibodies, pH, optical or magnetic signals, etc.[40]. Different materials have been used for the fabrication of these structures and various stimuli to trigger the release of the encapsulated molecules have been proposed. In this respect, biocompatibility and biodegradability have been regarded as essential properties for the application of such systems in drug delivery [41], [42].

Ultra-thin optical coatings with controllable color properties (UT-OCs): Ultra-thin film structures based on highly absorbent materials such as metals and semiconductors have gained massive interest lately[43]. Their advantages are related to the fact that a very strong optical interference can be obtained by thin-film coating an absorbent semiconductor material on a metal film, causing non-trivial phase changes in the reflected waves. This scheme allows the fabrication of ultra-thin coatings which are considerably thinner than conventional dielectric thin-film coatings. Moreover, in visible wavelengths, these ultra-thin films show structural colors with resonance dips, which can be changed with thickness variation and/or refractive index of coating materials.

Plasmonic Ceramic Nanoparticles (PCNPs): Transition metal nitrides and transition metal carbides are ceramics that are generally regarded as reliable solutions for surface coating as they are known to be mechanically hard materials. Another characteristic feature of these materials is their high carrier concentrations and metallic band structures. Thus, transition metal nitrides, particularly for titanium nitride (TiN) has been used in CMOS technology as gate layer and barrier material. On the other hand, the optical properties of these materials are also attractive. As their carrier concentrations are high, reaching to the order of 10^{22} cm^{-3}, nanostructures made of these materials can exhibit plasmon resonance peaks in the visible or near-infrared range. The plasmonic properties of nitrides and carbides have been studied in the past [44-46], and gain increasing attention as the fields of plasmonic metamaterials grows by the minute[47]. In particular, nitrides have become one of the most studied alternative plasmonic materials[36, 48-49]. Additionally, due to their broad optical absorption enhanced by the plasmon resonances, these materials have gained massive interest given their utility for applications that rely on photoelectric and photothermal conversions, e.g. visible-enhanced photocatalysis and solar heating [36-37, 50].

2. Experimental

2.1 Sample Synthesis and Preparation

2.1.1 Synthesis of DEX/PARG PMCs

In the present work, self-degrading PMCs were fabricated by the layer-by-layer self-assembly of a biopolymeric shell onto sacrificial templates[51-53] loaded with a proteolytic enzyme, **Fig. 1.** Namely, the proteolytic enzyme papain was co-precipitated into porous calcium carbonate microparticles (4-7 μm)[34, 54]. The enzyme loaded microparticles were used as templates for the fabrication of PMCs. Namely, $CaCO_3$ microparticles were alternately immersed in the anionic polysaccharide dextran (DEX) and in the cationic polypeptide polyarginine (PARG) solutions at 0.5 mg/mL in 0.15 M NaCl for 15 minutes under mild agitation. After each deposition step, the microparticles-polyelectrolyte suspension was washed three times with ultrapure water. A total of three DEX/PARG bilayers were deposited onto the microparticles surface. The microparticles were then dissolved by their dispersion in EDTA (0.2 M, pH 7) resulting in protein loaded PMCs. The self-degradation reaction of the protein-loaded PMCs was started immediately after the complete removal of the $CaCO_3$ templates and was carried out by incubating the PMCs suspension at 37 °C for a total of 12 hours. The degradation was characterized by s-SNOM and AFM imaging, as shown further in the Results section. Namely, 20 μl of protein loaded PMCs suspension were withdrawn after 1, 6 and 12 hours of reaction, deposited onto glass slides by drop-casting and let dry at room temperature for characterization. As control samples, unloaded PMCs were fabricated using plane calcium carbonate microparticles as sacrificial templates[55] and were incubated as well.

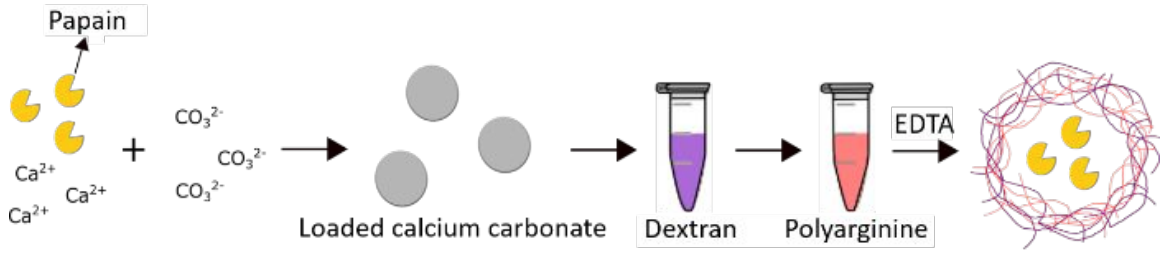

Figure 1 Process of fabrication of enzyme-loaded polyelectrolyte microcapsules.

2.1.2 Synthesis of Ti/Au/Ge UT-OCs

In this experiment we characterized Ti/Au/Ge UT-OCs deposited on a Si substrate using a strategy that combines electron beam evaporation and oblique angle deposition (OAD) as described by Yoo et al.[35]. These UT-OCs exhibit controllable color properties depending on the porosity of the topmost (Ge) layer[35]. Prior to depositing the Au film, a Ti layer with a thickness of 10 nm was deposited on the Si substrate to act as an adhesive layer. The Au film was deposited at a rate of ~2 Å/s under a pressure of ~10^{-6} torr; the Au layer had a thickness of 100 nm (sufficient optical thickness). Ge thin-films were further on deposited on the Au film with inclined sample holders at two different angles (0° and 70°) at a rate of ~1 Å/s under a pressure of ~10^{-6} torr (**Fig. 2 (b,d)**). 10 and 25 nm thicknesses of the Ge films were used for both deposition angles. To simulate defects, a hole pattern array (**Fig. (2.a)**) was fabricated in lift-off process with OAD, a technique that basically combines a typical deposition system, such as an electron beam evaporator or thermal evaporator, with a tilted substrate. The oblique angle of incident flux creates atomic shadowing, which produces areas that the vapor flux cannot reach directly[56].

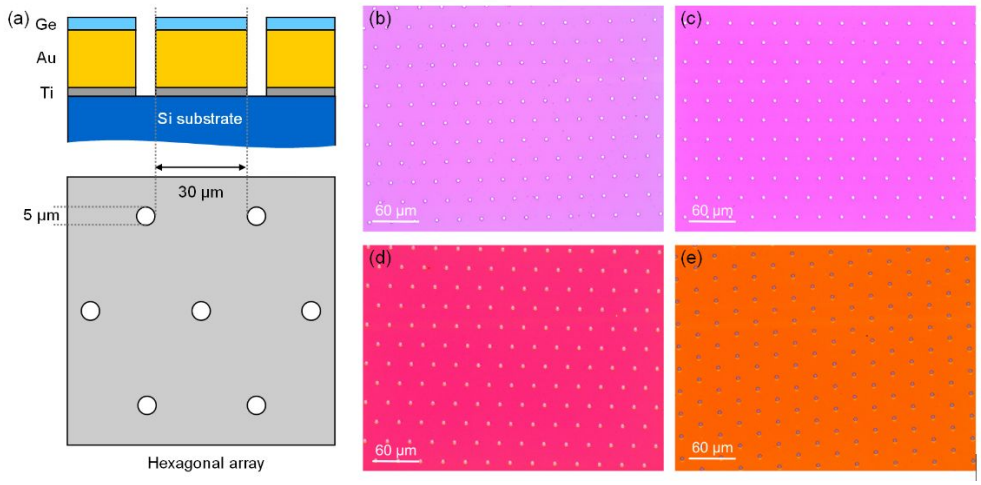

Figure 2 (a) Schematic illustrations of ultra-thin films with hole pattern array. (b-e) Brightfield microscope images of hole-patterned samples with different deposition angles (0, 30, 45, and 70°) at a thickness of 15 nm, respectively.

2.1.3 Preparation of PCNPs for imaging

In this experiment we have investigated two types of PCNPs: (i) titanium nitride (TiN) nanoparticles (NPs) and titanium carbide (TiC) nanoparticles (NPs). TiN NPs were synthesized with a thermal plasma method in argon and nitrogen plasma using titanium power[57] and the TiC NPs were synthesized in argon-hydrogen using a mixture of alcohol and titanium dioxide power[57]. Each of the NPs were dispersed into ethanol and spin-coated on quartz substrates. In **Fig. 3** we illustrate TEM images of the so synthesized TiN and TiC NPs.

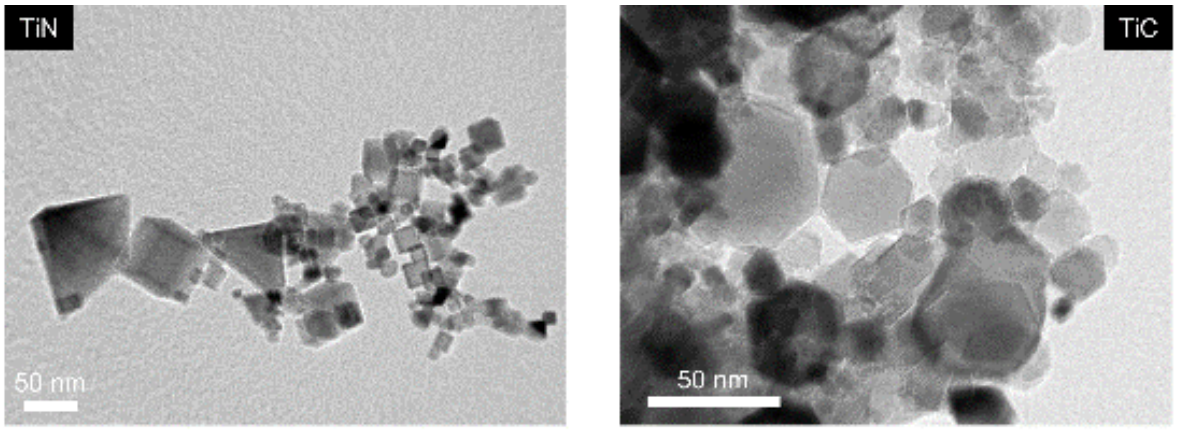

Figure 3 TEM Images of the investigated TiN (left) and TiC (right) NPs

2.2 Imaging Configurations and Methods

2.2.1 s-SNOM imaging setup and acquisition configuration

A diagram of the s-SNOM system used in this experiment is presented in Fig. 4. This architecture was built in-house, as an upgrade to an Q-scope 350 Atomic Force Microscope (Quesant, USA), and is configured to perform in a pseudoheterodyne detection scheme. In this detection strategy the optical signals of interest are extracted from the intense background light using a SR844 RF lock-in amplifier (Stanford Research Systems, USA), locked on successive harmonics of the pseudoheterodyned signal[58], **Fig. 4**. In s-SNOM, to ensure consistent image acquisition, the probe needs to remain in a fixed position with respect to the excitation beam for this latter to remain focused on the tip apex while near-field data is collected. In the developed configuration this was achieved by replacing the original xy probe scanning system of the Q-scope 350, with an xy sample scanning system consisting in a MCLS03113 piezoceramic stage (MadCityLabs, USA). For s-SNOM excitation we used a 638 nm semiconductor laser (Omicron, Germany), with 60 μW power (measured after the objective); the focal spot of the circularly polarized beam was aligned with the position of the probe through a long working distance objective (50x, 0.42 N.A.). In the

case of s-SNOM the tip's radius of curvature dictates the maximal attainable resolution on the xy-plane. The MikroMasch™ NSC19/Ti-Pt probe used in our experiments (Innovative Solutions Bulgaria Ltd) has a radius of curvature in the tip's apex <35 nm, a tip height of 20-25 μm and a full tip cone angle <30. Optical near-field signals were collected using the same objective used for excitation and were directed onto a photodiode connected to the SR844 RF lock-in amplifier, locked on two successive harmonics of the signal, which facilitates the extraction of optical signals of interest from the intense background. This home-made system was previously demonstrated in various experiments focused on the characterization of materials and biological samples. [26, 29, 59-60].

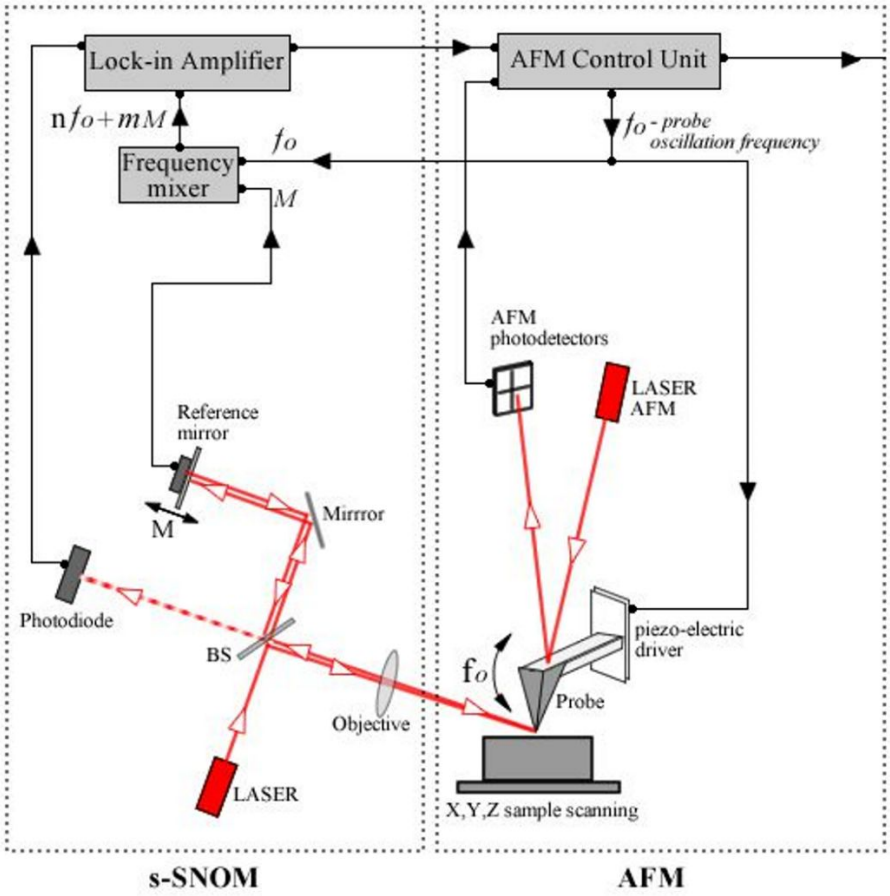

Figure 4. Homebuilt s-SNOM experimental setup. (a) The s-SNOM setup is based on a pseudoheterodyne detection configuration, consisting in a modified Michelson interferometer with one interferometer arm focused onto the tip and the other one reflected off a harmonic oscillating reference mirror. The reference beam interferes with the scattered light originated from the near-field of the sample and the interference signal contains the near-field information at frequencies $n \cdot fo \pm m \cdot M$, where f_o is the probe oscillation frequency, M is the mirror oscillation frequency and n, m are integers. The s-SNOM signal is collected using a lock-in amplifier locked at the $n \cdot fo \pm m \cdot M$ spectral harmonics.

2.2.2 Mapping the dielectric function with s-SNOM

For mapping the complex dielectric function of the three considered materials, we processed s-SNOM images in association with the Oscillating Point Dipole (OPD) model, which defines the dependency of the scattered light intensity on the electric permittivity. In the method introduced to achieve this purpose by D.E. Tranca et al.[31], a reference material (the substrate, or some other known material present in the field-of-view) is required to enable permittivity mapping of the materials/objects of interest. In the present work we employed an improved way for precisely defining the location of the reference material in the s-SNOM images. While in our previous approach[31] the reference material was selected based on a user-defined threshold height from the topography map collected by Atomic Force Microscopy (AFM), in the present work the reference material is selected based on a region-of-interest (ROI) defined by user in the topography map. The ROI area can be modified by the user and it can be rectangular, square, circle or ellipse. This improvement increases the measurement sensitivity due to a more precise assignation of the reference material location.

Another improvement of the method is related to the employed algorithm. Previously, the theoretical amplitudes and phases were calculated for a large pre-defined complex electric permittivity matrix, which was afterwards used to perform a calibration step using the experimental amplitudes and phases for the reference material[31]. In the current approach, the computational time was improved by calculating only the theoretical magnitudes of two successive harmonic components of the theoretical s-SNOM signal's spectrum, without calculating anymore the theoretical amplitudes and phases, which would require two additional computational steps. The corresponding experimental magnitudes of the same spectral components are easily obtained from the original s-SNOM images. After the calibration, the s-SNOM images were converted into complex permittivity maps pixel-by-pixel.

2.2.2 In-situ AFM analysis of the DEX-PARG film

A Keysight 5500 AFM system was used to investigate how the morphology of the three DEX-PARG bilayers (representing the PMCs shell) evolves in real-time when immersed in papain at 37 °C. Specifically, the bilayers were deposited onto silicon slides, immersed in papain solution and subjected to imaging at room temperature conditions. Afterwards, the temperature was raised at 37°C (controlled by a Peltier junction) and monitored by a type-K thermocouple. The bilayers were again subjected to imaging after 2h of degradative reaction. The conducted AFM measurements were performed in non-contact mode. In this workmode, after immersing the scanner inside the solution, the resonant frequency was reduced with a factor of ~3 and fine tuning was performed to identify the proper working condition of the cantilever.

3. Results & Discussions

The purpose of this experiment was to exploit s-SNOM's capabilities for determining the complex permittivity of nanostructured materials (or connected optical parameters) in the frame of precise applications focused on three distinct types of advanced materials: microcapsules assembled with layer-by-layer strategies for drug-delivery, ultra-thin optical coatings with tunable color properties, and plasmonic ceramic nanoparticles. The results obtained in the case of the three considered advanced materials are discussed in the following.

3.1 Complex permittivity mapping of PMCs

The potential usefulness of these PMCs for drug-delivery has been discussed in detail in previous works [34, 61-63]. Imaging methods are very important to design and develop efficient strategies to functionalize PMCs, and light microscopy techniques have been demonstrated as valuable tools for elucidating various PMC-related aspects[64]. In our previous work we qualitatively showed that s-SNOM has the potential to resolve optical details not available with diffraction limited techniques[60]. In the current experiment, we have focused our attention on the quantitative s-SNOM imaging of a specific class of PMCs, namely biopolymeric capsules that can self-degrade in a controlled fashion upon the interaction of an entrapped proteolytic enzyme with the PMC walls. This experiment extends previous recent work[34], where it was shown by confocal microscopy and AFM how enzymes loaded inside such microcapsules disrupt the microcapsules shell. The investigation and evaluation of the degradative process plays a pivotal role for the design of efficient delivery systems, however considering the dimensions of the microcapsules, and the scale at which degradation cues occur, this process is impossible to be optically investigated in detail with diffraction limited techniques. In the current experiment s-SNOM was used to investigate modifications in the complex permittivity of PMCs' surface, at different time points during the degradation process. These modifications are linked to a change in the composition/consistency of the PMCs' walls and have a direct impact over their efficiency as agents for controlled drug-release. s-SNOM was thus used to monitor how the degradation process evolves in time at optical resolutions beyond the diffraction barrier. In **Fig. 5** we present images collected on self-degrading PMCs at different time points (1, 6 and 12h), and of control PMC capsules, without entrapped enzyme.

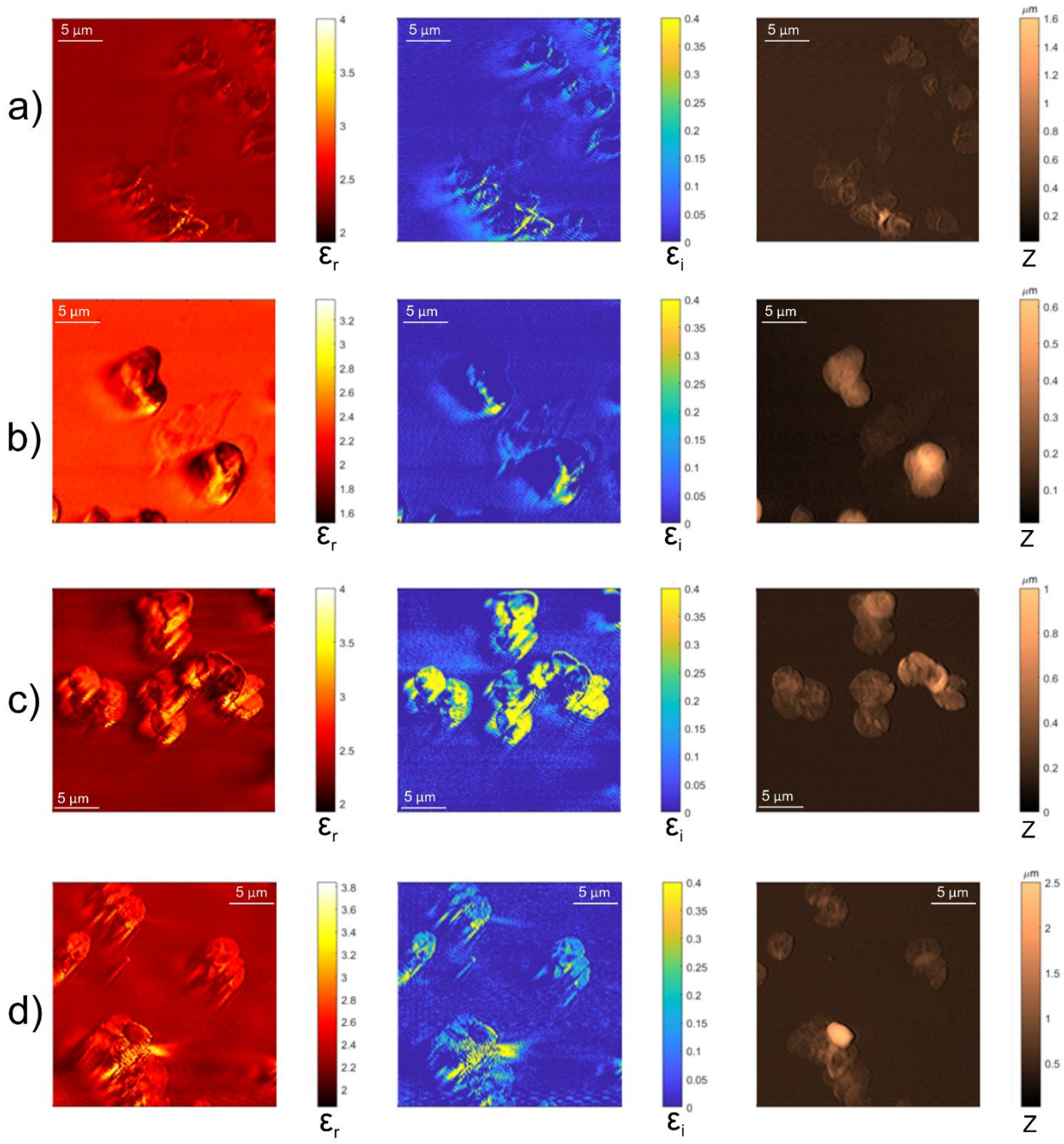

Figure 5. Complex permittivity and topography maps of dextran and polyarginine PMCs a) without entrapped enzymes, degraded by papain after b) 1h, c) 6h and d) 12h. Complex permittivity maps are calculated based on s-SNOM data, topography maps are collected with AFM.

Papain was chosen as degrading enzyme due to its wide use in different applications, spanning from food to pharmaceutical industries[65]. Moreover, it should be taken into account that papain, being a proteolytic enzyme, degrades only the polypeptidic component of the multilayer (PARG), leaving intact the

polysaccharide DEX. Recently Boi et al. demonstrated the release of polymeric nanoparticles from DEX/PARG microcapsules loaded with papain[34]. Namely, they demonstrated that after 2 hours of degradative reaction nanoparticles start to be released. Moreover, they demonstrated by confocal microscopy that after 12 hours of degradation PMCs were still present, but their spherical shape was lost, and large cracks and frayed edges were present. The results of the current experiment show that such cracks and frayed edges become noticeable after only 6 h of degradation and confirm that the PMCs are not destroyed upon 12 h degradation. Moreover, complex permittivity mapping with s-SNOM provides additional optical cues of how the PMCs structure is modified along the degradation process. Namely, control PMCs (**Fig. 5a**) showed a homogeneous ε_r indicating that the composition of the external layer of the PMCs remains consistent. As presented in more detail in Section 2, the imaged PMCs were made of dextran and polyarginine, where the last (exposed) layer is polyarginine. It is important to mention though that a net separation between the different layers does not exist, as the consecutive layers intertwine when deposited[66-67]. Moreover, it should be noted that PMCs fragments were visible into the control sample. This fact has already been reported into the literature specifically for biopolymeric capsules, which could break due to osmotic pressure caused by the dissolution of the core[68]. After 1 h of degradation, complex permittivity mapping showed a change in contrast in some areas of the PMCs, which could be ascribed to the initial degradation of the polyarginine component of the shell. As relates to topography, no evident changes were registered. As degradation proceeds, a change of $\varepsilon_r/\varepsilon_i$ contrast can be observed, **Fig. 5**, which indicates that the progressive degradation of polyarginine results into the reorganization of the surface layers. The degradation process was also characterized in real-time at 37 °C by AFM. Specifically, the DEX/PARG three bilayers, representing the PMCs shell, were deposited onto silicon slides and their real-time papain degradation was characterized by AFM in liquid at 37°C. Images of the samples were acquired after 2 hours of degradation reaction. In **Fig. 6**, we compare the DEX/PARG film in air and after the immersion in ultrapure water.

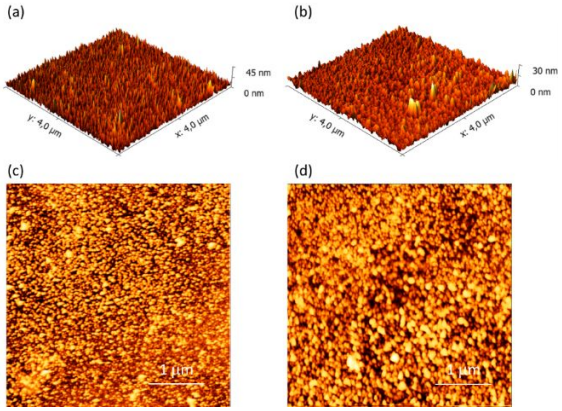

Figure 6. Topography of the DEX-PARG film: (a) and (c) topography of the pristine film; (b) and (d) report data after the immersion in ultrapure water.

The pristine sample is reported in **Fig. 6 (a), (c),** the former being a 3D representation of the surface to appreciate the film roughness. The morphology is in close agreement with the literature[63]. After the immersion, the film homogeneity is stable for hours suggesting that no damages occur on the film. Interestingly, we note that the sample topography is changed: in fact, grains increase their size due to a hydration after the immersion inside water. The situation significantly evolves if papain is added and the sample is kept at 37 °C, as reported in **Fig. 7**.

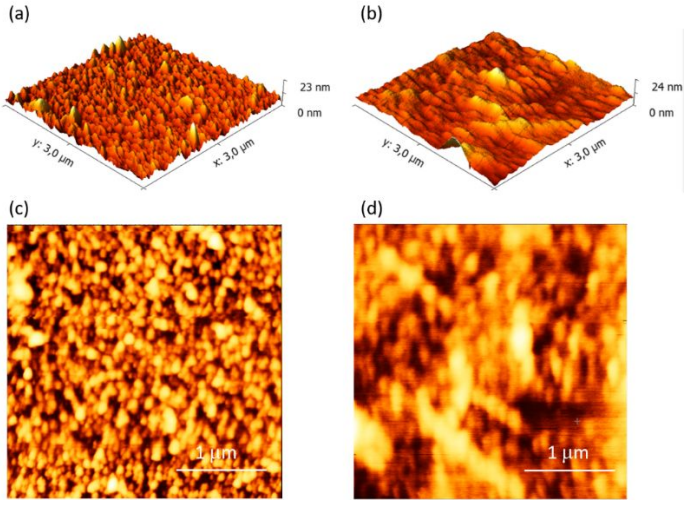

Figure 7 Topography of the DEX-PARG film. (a) and (c) refer to the film immersed in papain solution at room temperature, while (b) and (d) report data when the papain solution is kept at 37 °C.

When papain is added in the solution, and the sample is kept at room temperature, no significant changes in the DEX/PARG topography are observed (**Fig. 7 (a), (c)**). We can observe however that the film roughness is slightly reduced with respect to the previous case (see Fig. 6), which occurs due to ineffective activation of the enzymatic reaction at room temperature. Conversely, if the temperature is raised up to 37 °C and the sample is kept at this value for about 2 h, by AFM we can observe a significant alteration of the surface morphology. In particular, depression areas [darker regions in **Fig. 7 (b), (d)**] suggest that the DEX/PARG film is damaged due to the enzymatic effect of the papain in warm solution. These results confirm, on a smaller area, the degradation observed by the s-SNOM. Overall, the film integrity was not lost, supporting the continuous reorganization of the multilayer structure. This phenomenon was already reported into the literature for planar LbL films. Namely, Ren et al. showed that, upon enzymatic degradation, despite changes of the films' surface, these maintain their integrity[66]. This could be ascribed to a progressive erosion rather than a bulk deconstruction of the whole films. As already observed by Boi et al.[34] by confocal microscopy, our results confirmed that after 12 h of degradative reaction the PMCs were maintained. Moreover, the observed topography was similar to the one registered after 6 hours. As relates

to the complex permittivity contrast, the PMCs were found to be more homogeneous, which could indicate that polyarginine degradation and consequent rearrangement of the layers reached an overall stability.

Overall, the AFM and s-SNOM observation, together with the confocal microscopy results already published, allowed us to interpret the degradation mechanism. We can conclude that the different information obtained by using different microscopies could help in the interpretation of a complex mechanism, such as the proteolytic degradation of biopolymeric structures.

3.2 Permittivity and reflectance mapping of UT-OC

In a recent method Yoo et al.[35] introduced an efficient way of improving the color tunability and color purity of highly absorbent thin-films using porosity[35]. Namely, this methods relies on controlling the porosity of the deposited film using OAD, to achieve UT-OCs exhibiting different effective refractive indexes, which consequently allows the synthesis of UT-OCs with distinct optical characteristics. The architecture of the investigated Ti/Au/Ge optical coatings, schematically illustrated in **Fig. 2**, is similar to that proposed in the abovementioned study[35], where it was shown that modifications in the thickness of the topmost layer of this UT-OC and the angle at which it is deposited result in various reflectance/color characteristics, making the control of these properties very easy. Although practical results demonstrate the variation of the effective refractive index with the porosity by the calculation based on the volume averaging theory[69], the permittivity/refractive index of the fabricated ultra-thin porous samples is hard to measure with conventional methods such as ellipsometry at high lateral resolution. Furthermore, associated optical parameters whose assessment is important for determining the quality of the end product (e.g. reflectance), are difficult to map at nanoscale with conventional techniques. In **Fig. 8** we demonstrate that quantitative s-SNOM imaging has the potential to act as a solution to this problem as it can be used to map the dielectric function of ultra-thin porous films, and intrinsic optical properties, at resolutions similar to AFM. For this we imaged four instances of Ti/Au/Ge optical coatings: instances with the (topmost) Ge layer of 10 nm and 25 nm under deposition angles of 0° and 70°. In each of the synthesized specimens, holes of 5 μm in diameter, reaching the Si substrate, have been fabricated in a patterned array to better illustrate the capacity of s-SNOM to assess defects in such UT-OC that reflect in complex permittivity inhomogeneities (and connected optical parameters) across their surface. In Fig. 8, we show s-SNOM's capacity to illustrate in a quantitative manner permittivity/reflectance variation across the four specimens produced this way. The reflectance maps have been derived from the specimens' complex refractive index as shown in Eq. 1, and discussed in[35]:

$$Reflectance = \frac{r_{12} + r_{23}e^{2i\beta}}{1 + r_{12}r_{23}e^{2i\beta}}, \quad (Eq.1)$$

Where $r_{pq} = (\tilde{n}_p - \tilde{n}_q)/(\tilde{n}_p + \tilde{n}_q)$, with $\tilde{n}_p = n_p + ik_p$ and $\beta = (2\pi/\lambda)\tilde{n}_2 h$. Exact values of the complex refractive index were extracted from s-SNOM data as shown in[32].

The Reflectance maps shown in **Fig. 8** demonstrate that s-SNOM can be regarded as a very important tool for the quality verification and validation of UT-OCs. It can quantitatively map their optical properties at subdiffraction lateral resolutions that do not depend on the excitation wavelength but solely on the dimension of the tip used for scanning. The results presented in **Fig. 8**, show that each thickness-deposition angle combination of the topmost Ge layer results in different optical properties of the Ti/Au/Ge UT-OCs in terms of reflectance. The reflectance variations induced by distinct depositions angles for the Ti/Au/Ge UT-OCs possessing 10 nm Ge layers are lower compared to those observed in the UT-OC instances that were with synthesized with a 25 nm Ge layer; these results are in agreement with previous work [35]. Interestingly, we can observe that in the case of the defects that were intentionally induced with the lift-off process described in Section 2.1.2, the correspondence between the topography and the reflectance maps is not exact. The reflectance of the films seems to be affected not only in the defect area noticeable in the topography map, but also in close proximity (especially visible in **Fig. 8c**), which brings an additional insight compared to the case in which these defects would have been solely characterized with AFM. This suggests that local reflectance mapping with s-SNOM at nanoscale resolutions can provide complementary information over other nanoscale capable techniques in terms of UT-OC quality assessment and defect characterization. Achievable resolutions can reach 1 nm with ultra-sharp s-SNOM probes[70], a scale impossible to address locally with other optical instruments capable of refractive index mapping. Furthermore, considering recent progress in other related methods, e.g. Tip Enhanced Raman Scattering, where sub-nanometer resolutions where demonstrated[4] in breakthrough experiments carried out over the past decade, we are inclined to believe that it will not be long before similar resolutions will also be available/possible for s-SNOM.

Considering the huge potential of these new generation UT-OCs materials for the mobile and wearable devices markets (as a result of their capacity to reproduce a wide palette of colors) we argue that s-SNOM's capacity to map their optical properties at nanoscale (and, soon probably even beyond) is indeed very valuable. Such s-SNOM approaches can be used to determine the homogeneity of optical properties of UT-OCs and identify defects (or features of interest) not observable with diffraction limited techniques. The fact that s-SNOM and AFM images can be collected simultaneously, is also an important asset of s-SNOM imaging as this approach allows placing optical data in a well understood topographic context. Furthermore, in-tandem s-SNOM and AFM imaging allows a correlative analysis of the the relationships that take place between the UT-OCs' morphological structure and their optical properties, which is also of interest in many applications.

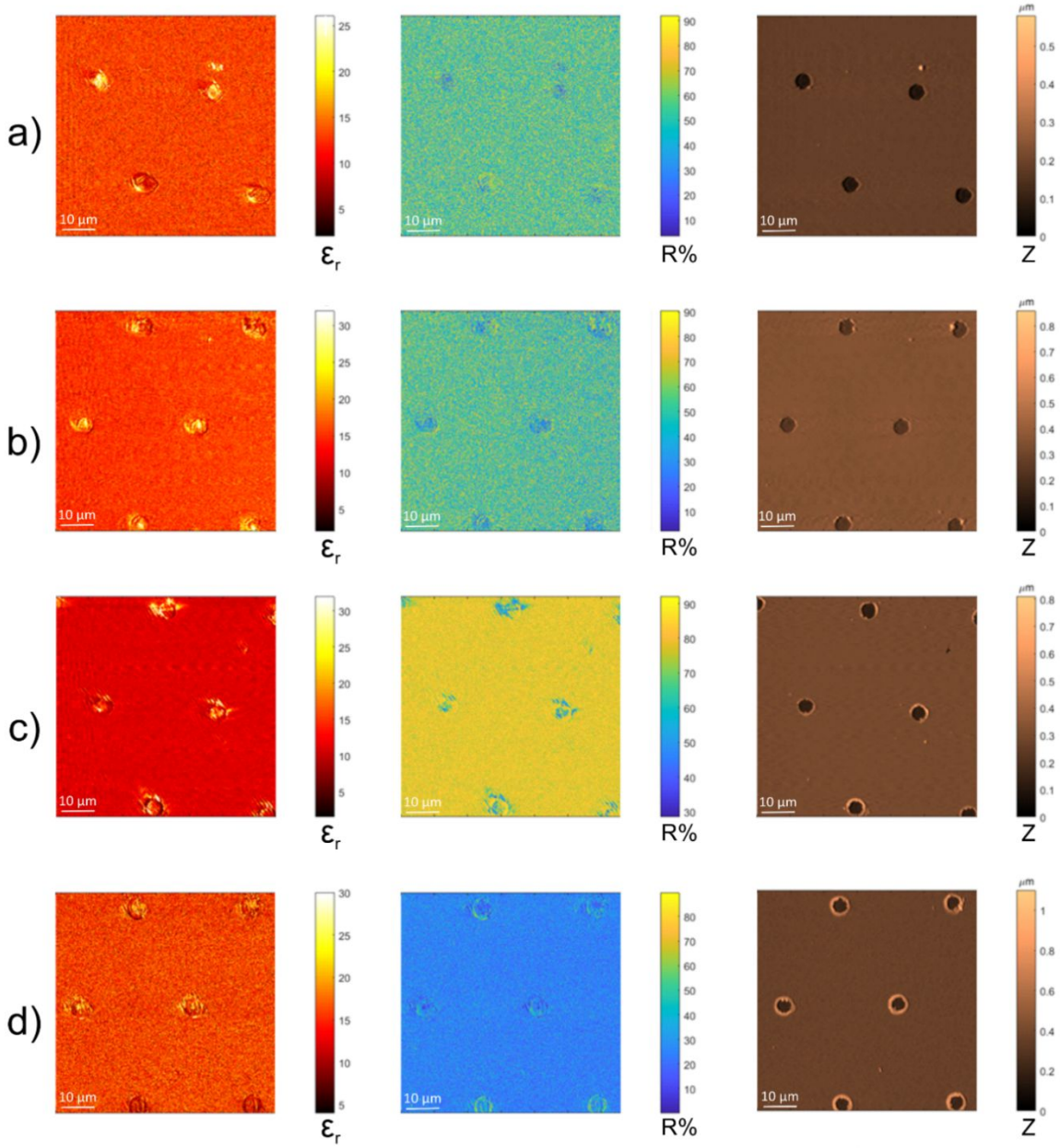

Fig. 8 Permittivity, reflectance and topography maps of Ti/Au/Ge UT-OCs. a) and b) depict samples with a 10 nm Ge layer deposited under a deposition angle of 0° and 70°, respectively. c) and d) depict samples with a 25 nm Ge layer deposited under a deposition angle of 0° and 70°, respectively. Permittivity and reflectance maps are calculated based on s-SNOM data; topography maps are collected with AFM.

3.3 Complex permittivity mapping of PCNPs

We investigate with quantitative s-SNOM the complex permittivity of two PCNPs: TiC and TiN NPs. Similar to the situation of metals, the plasmon resonances of nitride- and carbide-based nanomaterials are

sensitive to their nanoscale geometry and their permittivities. Evaluating the latter is thus vital for accurately designing such nanostructures, and for assessing their performance. Nitrides and carbides nanostructures can be fabricated through various techniques. For the top-down fabrication processes which start from thin film, the permittivity of the thin film can be obtained by an ellipsometer (with low lateral resolution, though). On the other hand, in the case of bottom-up processes, measuring the exact complex permittivity of resulted nanostructures, such as nanoparticles or nanorods, is often quite difficult. In **Fig. 9**, we demonstrate s-SNOM's potential to act as a solution to this problem and provide quantitative information on the complex permittivity of distinct CPNP's structures. We present complex permittivity maps calculated on TiN and TiC NPs, that have been synthesized as detailed in the Methods section. The sizes of the NPs obtained from the s-SNOM are comparable to the TEM images shown in **Fig. 3.** To explain the dimension of the TiN and TiC structures that can be noticed in the images of **Fig. 9**, we refer to previous studies conducted with the help of dynamic light scattering (DLS) which demonstrated that TiN/TiC NPs tend to aggregate in liquids. **Fig. 9a**) shows negative values for the ε_r of TiN NPs at the measured wavelength (638 nm), which indicates metallic properties; we find important to observe that clustering does not result in formations with positive ε_r. The ε_i values of the imaged TiN NPs clusters take values >1, and it can be noticed that both ε_i and ε_r measured based on s-SNOM data take different values depending on the size of the imaged NP clusters. Hence, we can argue that s-SNOM can be used to measure the actual permittivity and dielectric loss factor of distinct PCNPs structures [36], and eventually to measure the strength of the plasmon resonances that occur in such structures at different illumination wavelengths. Such capabilities of s-SNOM are demonstrated also in the case of TiC NPs, **Fig. 9b**. Their performance in applications for photocatalysis and photothermal heating are directly dependent on their size and dielectric function[36], properties easy to assess with the AFM/s-SNOM tandem as shown in **Fig. 9b)**, and in **Fig. 10**; in this latter figure we emphasize on the potential of s-SNOM to quantitatively map the complex permittivity of PCNP clusters depicting a segmented s-SNOM/AFM data set, and mean permittivities for segmented structures of a particular size. In the AFM topography images in **Figs 9b)** and **Fig 10** we can observe that the TiC nanoparticles aggregated and formed clusters, with sizes up to the order of microns. The existing differences in the complex permittivities of the observable TiC structures could be due to slight variations between the particles and the strength of the scattering. Considering that a precise understanding and assessment of the complex permittivity/optical characteristics and behavior of PCNPs at nanoscale resolutions is key for optimizing their performance in applications addressing various fields, we argue that s-SNOM represents an important tool for their study.

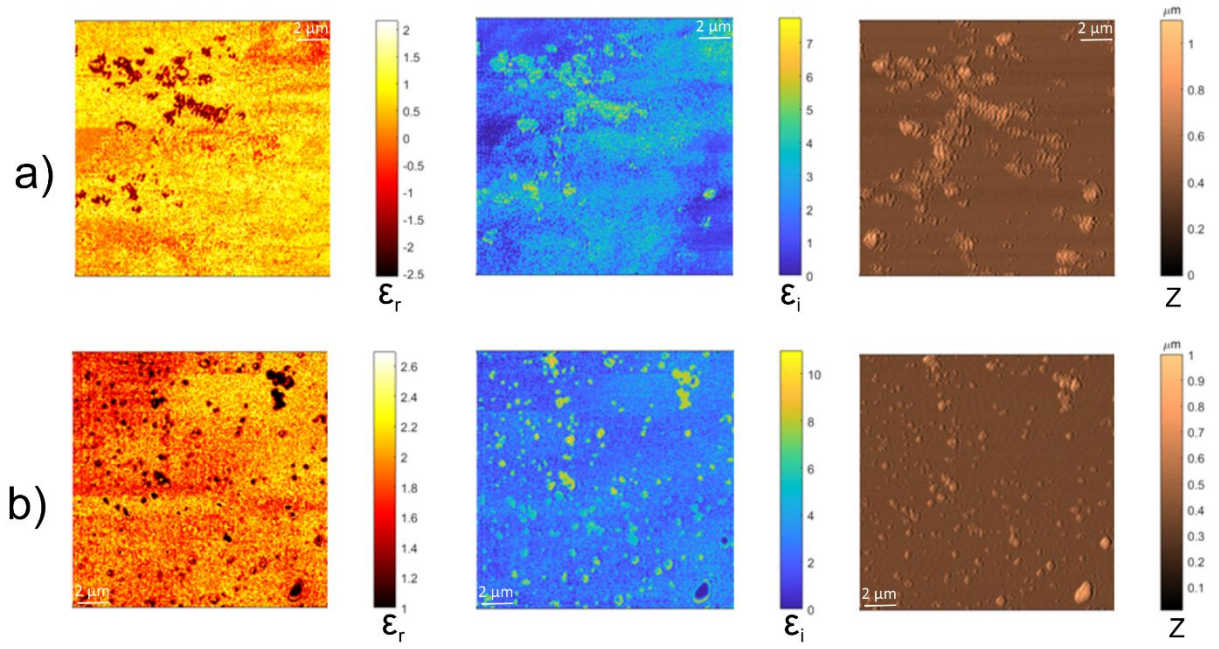

Fig. 9. Complex permittivity and topography maps of a) TiN and b) TiC NP clusters.

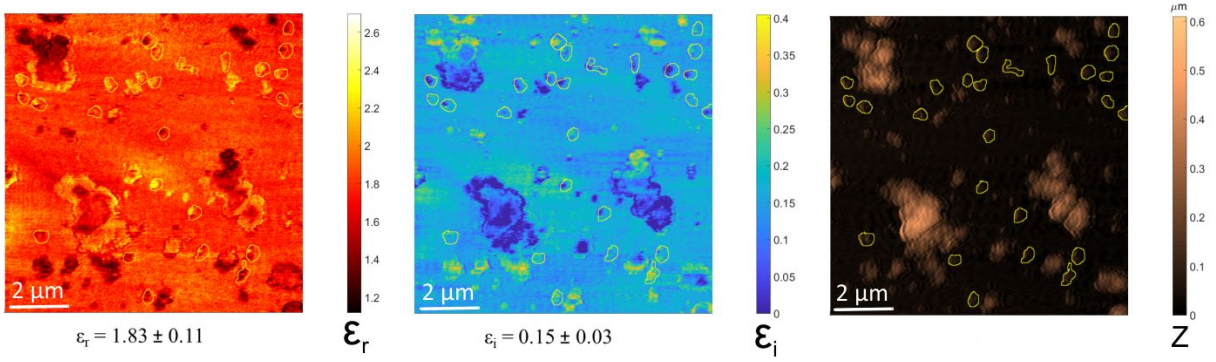

Fig. 10. Segmented topography and complex permittivity maps of TiC NP clusters in a 10x10 µm² imaged area. Segmentations masks were computed on the AFM image for TiC formations with an area of particular size *s*, where 0.1 µm²<*s*<0.2 µm² and were imposed on the complex permittivity maps derived from s-SNOM data. Mean $\varepsilon_r/\varepsilon_i$ values are provided for the segmented TiC NP structures.

4. Conclusions

In this experiment we have performed complex permittivity mapping with s-SNOM on three distinct types of nanostructured materials: microcapsules assembled with layer-by-layer strategies for drug-delivery, ultra-thin optical coatings with tunable color properties, and ceramic plasmonic nanoparticles. The results show that imaging approaches that combine s-SNOM optical data and the OPD model to extract quantitative information over the complex permittivity and associated optical properties, have the potential to be of great

help for characterizing these advanced materials (and similar ones). In the case of the investigated PMCs assembled from consecutively deposited charged dextran and polyarginine layers, we observed that complex permittivity mapping with s-SNOM can provide optical cues on how the PMC structure is modified in the case of a model relevant for controlled enzyme-degradation. For Ti/Au/Ge ultra-thin films we have shown that s-SNOM imaging is useful for assessing the optical homogeneity/quality of such coatings, as optical parameters that can be derived from the real and imaginary parts of the dielectric function, e.g. reflectance, are also available with this technique. In the case of TiN and TiC NPs, an exact assessment of the complex permittivity for distinct instances, or clusters, is important for evaluating their behavior and performance. Our experiment demonstrated that measuring these properties is possible with quantitative s-SNOM, which represent an important tool in the quest for understanding in detail the optical properties of these emerging advanced materials. While the conducted experiments employed illumination with a single wavelength, the discussed method for mapping the complex permittivity at nanoscale resolutions depending solely on the size of the tip, can be used in association with broadband/tunable lasers for spectroscopic investigations over the dielectric function. Overall, the presented results are meant to facilitate the penetration of complex permittivity mapping with s-SNOM in nanomaterials science, nanomedicine and nanophotonics and pave the way for novel characterization approaches and applications.

Acknowledgments

S.G. Stanciu and his colleagues at UPB acknowledge the support of the Romanian Executive Agency for Higher Education, Research, Development and Innovation (UEFISCDI) via grants PN-III-P1-1.1-TE-2016-2147 (CORIMAG) and PN-III-P3-3.1-PM-RO-CN-2018-0177 (NANOMATBIOIMAGE). Y.M. Song and Y.J. Yoo's work was supported by the National Research Foundation (NRF) of Korea (NRF-2018R1A4A1025623). S. Ishii contribution was supported by the JSPS KAKENH Grant Number 17H04801, 19H04331, TEPCO Memorial Foundation. F. Yang acknowledges Inter-Governmental S&T Cooperation project between China-Romania funded by the Ministry of Science and Technology of China (department of International Cooperation).

References

(1) Schermelleh, L.; Ferrand, A.; Huser, T.; Eggeling, C.; Sauer, M.; Biehlmaier, O.; Drummen, G. P. Super-resolution microscopy demystified. *Nature cell biology* **2019,** *21* (1), 72.
(2) Chen, X.; Hu, D.; Mescall, R.; You, G.; Basov, D.; Dai, Q.; Liu, M. Modern Scattering-Type Scanning Near-Field Optical Microscopy for Advanced Material Research. *Advanced Materials* **2019**, 1804774.
(3) Gerton, J. M.; Wade, L. A.; Lessard, G. A.; Ma, Z.; Quake, S. R. Tip-enhanced fluorescence microscopy at 10 nanometer resolution. *Physical Review Letters* **2004,** *93* (18), 180801.

(4) Zhang, R.; Zhang, Y.; Dong, Z.; Jiang, S.; Zhang, C.; Chen, L.; Zhang, L.; Liao, Y.; Aizpurua, J.; Luo, Y. e. Chemical mapping of a single molecule by plasmon-enhanced Raman scattering. *Nature* **2013,** *498* (7452), 82-86.
(5) Nowak, D.; Morrison, W.; Wickramasinghe, H. K.; Jahng, J.; Potma, E.; Wan, L.; Ruiz, R.; Albrecht, T. R.; Schmidt, K.; Frommer, J. Nanoscale chemical imaging by photoinduced force microscopy. *Science advances* **2016,** *2* (3), e1501571.
(6) Lu, F.; Jin, M.; Belkin, M. A. Tip-enhanced infrared nanospectroscopy via molecular expansion force detection. *Nature photonics* **2014,** *8* (4), 307-312.
(7) Wang, P.; Slipchenko, M. N.; Mitchell, J.; Yang, C.; Potma, E. O.; Xu, X.; Cheng, J.-X. Far-field imaging of non-fluorescent species with subdiffraction resolution. *Nature photonics* **2013,** *7* (6), 449-453.
(8) Zanini, G.; Korobchevskaya, K.; Deguchi, T.; Diaspro, A.; Bianchini, P. Label-Free Optical Nanoscopy of Single Layer Graphene. *ACS nano* **2019**.
(9) Tzang, O.; Pevzner, A.; Marvel, R. E.; Haglund, R. F.; Cheshnovsky, O. Super-resolution in label-free photomodulated reflectivity. *Nano letters* **2015,** *15* (2), 1362-1367.
(10) Gong, L.; Zheng, W.; Ma, Y.; Huang, Z. Saturated Stimulated-Raman-Scattering Microscopy for Far-Field Superresolution Vibrational Imaging. *Physical Review Applied* **2019,** *11* (3), 034041.
(11) Keilmann, F.; Hillenbrand, R. Near-field microscopy by elastic light scattering from a tip. *PHILOSOPHICAL TRANSACTIONS-ROYAL SOCIETY OF LONDON SERIES A MATHEMATICAL PHYSICAL AND ENGINEERING SCIENCES* **2004**, 787-806.
(12) Wang, H.; Wang, L.; Xu, X. G. Scattering-type scanning near-field optical microscopy with low-repetition-rate pulsed light source through phase-domain sampling. *Nature communications* **2016,** *7*.
(13) Taubner, T.; Hillenbrand, R.; Keilmann, F. Performance of visible and mid-infrared scattering-type near-field optical microscopes. *Journal of microscopy* **2003,** *210* (3), 311-314.
(14) Jacob, R.; Winnerl, S.; Fehrenbacher, M.; Bhattacharyya, J.; Schneider, H.; Wenzel, M. T.; Ribbeck, H.-G. v.; Eng, L. M.; Atkinson, P.; Schmidt, O. G. Intersublevel spectroscopy on single InAs-quantum dots by terahertz near-field microscopy. *Nano letters* **2012,** *12* (8), 4336-4340.
(15) Keilmann, F.; Huber, A. J.; Hillenbrand, R. Nanoscale conductivity contrast by scattering-type near-field optical microscopy in the visible, infrared and THz domains. *Journal of Infrared, Millimeter, and Terahertz Waves* **2009,** *30* (12), 1255-1268.
(16) Qazilbash, M. M.; Brehm, M.; Chae, B.-G.; Ho, P.-C.; Andreev, G. O.; Kim, B.-J.; Yun, S. J.; Balatsky, A.; Maple, M.; Keilmann, F. Mott transition in VO2 revealed by infrared spectroscopy and nano-imaging. *Science* **2007,** *318* (5857), 1750-1753.
(17) Amenabar, I.; Poly, S.; Nuansing, W.; Hubrich, E. H.; Govyadinov, A. A.; Huth, F.; Krutokhvostov, R.; Zhang, L.; Knez, M.; Heberle, J. Structural analysis and mapping of individual protein complexes by infrared nanospectroscopy. *Nature communications* **2013,** *4*.
(18) Westermeier, C.; Cernescu, A.; Amarie, S.; Liewald, C.; Keilmann, F.; Nickel, B. Sub-micron phase coexistence in small-molecule organic thin films revealed by infrared nano-imaging. *Nature communications* **2014,** *5*, 4101.
(19) Yoxall, E.; Schnell, M.; Nikitin, A. Y.; Txoperena, O.; Woessner, A.; Lundeberg, M. B.; Casanova, F.; Hueso, L. E.; Koppens, F. H.; Hillenbrand, R. Direct observation of ultraslow hyperbolic polariton propagation with negative phase velocity. *Nature Photonics* **2015,** *9* (10), 674.
(20) Chen, J. N.; Badioli, M.; Alonso-Gonzalez, P.; Thongrattanasiri, S.; Huth, F.; Osmond, J.; Spasenovic, M.; Centeno, A.; Pesquera, A.; Godignon, P.; Elorza, A. Z.; Camara, N.; de Abajo, F. J. G.; Hillenbrand, R.; Koppens, F. H. L. Optical nano-imaging of gate-tunable graphene plasmons. *Nature* **2012,** *487* (7405), 77-81, DOI: 10.1038/nature11254.
(21) Fei, Z.; Rodin, A. S.; Andreev, G. O.; Bao, W.; McLeod, A. S.; Wagner, M.; Zhang, L. M.; Zhao, Z.; Thiemens, M.; Dominguez, G.; Fogler, M. M.; Castro Neto, A. H.; Lau, C. N.; Keilmann, F.; Basov, D. N. Gate-tuning of graphene plasmons revealed by infrared nano-imaging. *Nature* **2012,** *487* (7405), 82-85, DOI: 10.1038/nature11253.
(22) Yao, Z.; Xu, S.; Hu, D.; Chen, X.; Dai, Q.; Liu, M. Nanoimaging and Nanospectroscopy of Polaritons with Time Resolved s-SNOM. *Advanced Optical Materials* **2019**, 1901042.
(23) Khatib, O.; Wood, J. D.; McLeod, A. S.; Goldflam, M. D.; Wagner, M.; Damhorst, G. L.; Koepke, J. C.; Doidge, G. P.; Rangarajan, A.; Bashir, R. Graphene-based platform for infrared near-field nanospectroscopy of water and biological materials in an aqueous environment. *ACS nano* **2015,** *9* (8), 7968-7975.
(24) Tranca, D.; Stanciu, S.; Hristu, R.; Witgen, B.; Stanciu, G. A. Nanoscale mapping of refractive index by using scattering-type Scanning Near-Field Optical Microscopy. *Nanomedicine: Nanotechnology, Biology and Medicine* **2017**.
(25) Brehm, M.; Taubner, T.; Hillenbrand, R.; Keilmann, F. Infrared spectroscopic mapping of single nanoparticles and viruses at nanoscale resolution. *Nano Letters* **2006,** *6* (7), 1307-1310.

(26) Stanciu, S. G.; Tranca, D. E.; Hristu, R.; Stanciu, G. A. Correlative imaging of biological tissues with apertureless scanning near-field optical microscopy and confocal laser scanning microscopy. *Biomedical optics express* **2017,** *8* (12), 5374-5383.
(27) Lewin, M.; Hauer, B.; Bornhöfft, M.; Jung, L.; Benke, J.; Michel, A.-K.; Mayer, J.; Wuttig, M.; Taubner, T. Imaging of phase change materials below a capping layer using correlative infrared near-field microscopy and electron microscopy. *Applied Physics Letters* **2015,** *107* (15), 151902.
(28) Stiegler, J.; Tena-Zaera, R.; Idigoras, O.; Chuvilin, A.; Hillenbrand, R. Correlative infrared–electron nanoscopy reveals the local structure–conductivity relationship in zinc oxide nanowires. *Nature communications* **2012,** *3*, 1131.
(29) Tranca, D. E.; Sánchez-Ortiga, E.; Saavedra, G.; Martínez-Corral, M.; Tofail, S. A.; Stanciu, S. G.; Hristu, R.; Stanciu, G. A. Mapping electron-beam-injected trapped charge with scattering scanning near-field optical microscopy. *Optics letters* **2016,** *41* (5), 1046-1049.
(30) Kusch, P.; Mastel, S.; Mueller, N. S.; Morquillas Azpiazu, N.; Heeg, S.; Gorbachev, R.; Schedin, F.; Hübner, U.; Pascual, J. I.; Reich, S. Dual-scattering near-field microscope for correlative nanoimaging of SERS and electromagnetic hotspots. *Nano Letters* **2017,** *17* (4), 2667-2673.
(31) Tranca, D. E.; Stanciu, S. G.; Hristu, R.; Stoichita, C.; Tofail, S.; Stanciu, G. A. High-resolution quantitative determination of dielectric function by using scattering scanning near-field optical microscopy. *Scientific reports* **2015,** *5*, 11876.
(32) Tranca, D. E.; Stanciu, S. G.; Hristu, R.; Witgen, B. M.; Stanciu, G. A. Nanoscale mapping of refractive index by using scattering-type Scanning Near-Field Optical Microscopy. *Nanomedicine: Nanotechnology, Biology and Medicine* **2018,** *14* (1), 47-50.
(33) Pastorino, L.; Erokhina, S.; Erokhin, V. Smart nanoengineered polymeric capsules as ideal pharmaceutical carriers. *Current Organic Chemistry* **2013,** *17* (1), 58-64.
(34) Boi, S.; Dellacasa, E.; Bianchini, P.; Petrini, P.; Pastorino, L.; Monticelli, O. Encapsulated functionalized stereocomplex PLA particles: An effective system to support mucolytic enzymes. *Colloids and Surfaces B: Biointerfaces* **2019,** *179*, 190-198.
(35) Yoo, Y. J.; Lim, J. H.; Lee, G. J.; Jang, K.-I.; Song, Y. M. Ultra-thin films with highly absorbent porous media fine-tunable for coloration and enhanced color purity. *Nanoscale* **2017,** *9* (9), 2986-2991.
(36) Ishii, S.; Shinde, S. L.; Nagao, T. Nonmetallic Materials for Plasmonic Hot Carrier Excitation. *Advanced Optical Materials* **2019,** *7* (1), 1800603.
(37) Ishii, S.; Sugavaneshwar, R. P.; Nagao, T. Titanium nitride nanoparticles as plasmonic solar heat transducers. *The Journal of Physical Chemistry C* **2016,** *120* (4), 2343-2348.
(38) Sukhorukov, G. B.; Donath, E.; Davis, S.; Lichtenfeld, H.; Caruso, F.; Popov, V. I.; Möhwald, H. Stepwise polyelectrolyte assembly on particle surfaces: a novel approach to colloid design. *Polymers for Advanced Technologies* **1998,** *9* (10-11), 759-767.
(39) Richardson, J. J.; Björnmalm, M.; Caruso, F. Technology-driven layer-by-layer assembly of nanofilms. *science* **2015,** *348* (6233), aaa2491.
(40) Sukhorukov, G. B.; Möhwald, H. Multifunctional cargo systems for biotechnology. *TRENDS in Biotechnology* **2007,** *25* (3), 93-98.
(41) del Mercato, L. L.; Ferraro, M. M.; Baldassarre, F.; Mancarella, S.; Greco, V.; Rinaldi, R.; Leporatti, S. Biological applications of LbL multilayer capsules: From drug delivery to sensing. *Advances in colloid and interface science* **2014,** *207*, 139-154.
(42) Cui, W.; Li, J.; Decher, G. Self-Assembled Smart Nanocarriers for Targeted Drug Delivery. *Advanced Materials* **2016,** *28* (6), 1302-1311.
(43) Kats, M. A.; Blanchard, R.; Genevet, P.; Capasso, F. Nanometre optical coatings based on strong interference effects in highly absorbing media. *Nature materials* **2013,** *12* (1), 20.
(44) Steinmüller-Nethl, D.; Kovacs, R.; Gornik, E.; Rödhammer, P. Excitation of surface plasmons on titanium nitride films: determination of the dielectric function. *Thin Solid Films* **1994,** *237* (1-2), 277-281.
(45) Hibbins, A. P.; Sambles, J. R.; Lawrence, C. R. Surface plasmon-polariton study of the optical dielectric function of titanium nitride. *journal of modern optics* **1998,** *45* (10), 2051-2062.
(46) Schubert, W.; Shelton, R.; Wolf, E. Electron-energy-loss-and ultraviolet-photoemission-spectroscopy study of the VN x system. *Physical Review B* **1981,** *23* (10), 5097.
(47) Naik, G. V.; Shalaev, V. M.; Boltasseva, A. Alternative plasmonic materials: beyond gold and silver. *Advanced Materials* **2013,** *25* (24), 3264-3294.
(48) Guler, U.; Shalaev, V. M.; Boltasseva, A. Nanoparticle plasmonics: going practical with transition metal nitrides. *Materials Today* **2015,** *18* (4), 227-237.

(49) Patsalas, P.; Kalfagiannis, N.; Kassavetis, S. Optical properties and plasmonic performance of titanium nitride. *Materials* **2015,** *8* (6), 3128-3154.
(50) Ishii, S.; Chen, K.; Sugavaneshwar, R. P.; Okuyama, H.; Dao, T. D.; Shinde, S. L.; Kaur, M.; Kitajima, M.; Nagao, T. Efficient Absorption of Sunlight Using Resonant Nanoparticles for Solar Heat Applications. *Materials Nanoarchitectonics* **2018**, 241-253.
(51) Sukhorukov, G. B.; Donath, E.; Lichtenfeld, H.; Knippel, E.; Knippel, M.; Budde, A.; Möhwald, H. Layer-by-layer self assembly of polyelectrolytes on colloidal particles. *Colloids and Surfaces A: physicochemical and engineering aspects* **1998,** *137* (1-3), 253-266.
(52) Donath, E.; Sukhorukov, G. B.; Caruso, F.; Davis, S. A.; Möhwald, H. Novel hollow polymer shells by colloid-templated assembly of polyelectrolytes. *Angewandte Chemie International Edition* **1998,** *37* (16), 2201-2205.
(53) Volodkin, D. V.; Petrov, A. I.; Prevot, M.; Sukhorukov, G. B. Matrix polyelectrolyte microcapsules: new system for macromolecule encapsulation. *Langmuir* **2004,** *20* (8), 3398-3406.
(54) Delcea, M.; Möhwald, H.; Skirtach, A. G. Stimuli-responsive LbL capsules and nanoshells for drug delivery. *Advanced drug delivery reviews* **2011,** *63* (9), 730-747.
(55) Petrov, A. I.; Volodkin, D. V.; Sukhorukov, G. B. Protein—calcium carbonate coprecipitation: a tool for protein encapsulation. *Biotechnology progress* **2005,** *21* (3), 918-925.
(56) Hawkeye, M. M.; Brett, M. J. Glancing angle deposition: fabrication, properties, and applications of micro-and nanostructured thin films. *Journal of Vacuum Science & Technology A: Vacuum, Surfaces, and Films* **2007,** *25* (5), 1317-1335.
(57) Nakamura, K. Synthesis of nanoparticles by thermal plasma processing and its applications. *Earozoru Kenkyu* **2014,** *29* (2), 98-103.
(58) Tranca, D. E.; Stoichita, C.; Hristu, R.; Stanciu, S. G.; Stanciu, G. A. A study on the image contrast of pseudo-heterodyned scattering scanning near-field optical microscopy. *Optics express* **2014,** *22* (2), 1687-1696.
(59) Tranca, D. E.; Stanciu, S. G.; Hristu, R.; Stoichita, C.; Tofail, S.; Stanciu, G. A. High-resolution quantitative determination of dielectric function by using scattering scanning near-field optical microscopy. *Scientific reports* **2015,** *5*.
(60) Stanciu, S. G.; Tranca, D. E.; Ruggiero, C.; Stanciu, G. A.; Dellacasa, E.; Antipov, A.; Hristu, R.; Pastorino, L. Combined far-field, near-field and topographic imaging of nano-engineered polyelectrolyte capsules. *Materials Letters* **2016,** *183*, 105-108.
(61) Borodina, T.; Markvicheva, E.; Kunizhev, S.; Möhwald, H.; Sukhorukov, G. B.; Kreft, O. Controlled release of DNA from self-degrading microcapsules. *Macromolecular rapid communications* **2007,** *28* (18-19), 1894-1899.
(62) Marchenko, I.; Yashchenok, A.; Borodina, T.; Bukreeva, T.; Konrad, M.; Möhwald, H.; Skirtach, A. Controlled enzyme-catalyzed degradation of polymeric capsules templated on CaCO3: Influence of the number of LbL layers, conditions of degradation, and disassembly of multicompartments. *Journal of controlled release* **2012,** *162* (3), 599-605.
(63) Cardoso, M. J.; Caridade, S. G.; Costa, R. R.; Mano, J. o. F. Enzymatic degradation of polysaccharide-based layer-by-layer structures. *Biomacromolecules* **2016,** *17* (4), 1347-1357.
(64) Pastorino, L.; Dellacasa, E.; Noor, M. R.; Soulimane, T.; Bianchini, P.; D'Autilia, F.; Antipov, A.; Diaspro, A.; Tofail, S. A.; Ruggiero, C. Multilayered polyelectrolyte microcapsules: interaction with the enzyme cytochrome C oxidase. *PloS one* **2014,** *9* (11), e112192.
(65) Homaei, A.; Samari, F. Investigation of activity and stability of papain by adsorption on multi-wall carbon nanotubes. *International journal of biological macromolecules* **2017,** *105*, 1630-1635.
(66) Ren, K.; Ji, J.; Shen, J. Construction and enzymatic degradation of multilayered poly-L-lysine/DNA films. *Biomaterials* **2006,** *27* (7), 1152-1159.
(67) Serizawa, T.; Yamaguchi, M.; Akashi, M. Time-controlled desorption of ultrathin polymer films triggered by enzymatic degradation. *Angewandte Chemie International Edition* **2003,** *42* (10), 1115-1118.
(68) Chojnacka-Górka, K.; Rozpędzik, A.; Zapotoczny, S. Robust polyelectrolyte microcapsules reinforced with carbon nanotubes. *Rsc Advances* **2016,** *6* (115), 114639-114643.
(69) Garahan, A.; Pilon, L.; Yin, J.; Saxena, I. Effective optical properties of absorbing nanoporous and nanocomposite thin films. *Journal of applied physics* **2007,** *101* (1), 014320.
(70) Zenhausern, F.; Martin, Y.; Wickramasinghe, H. Scanning interferometric apertureless microscopy: optical imaging at 10 angstrom resolution. *Science* **1995,** *269* (5227), 1083-1085.

Graphical Table of Contents

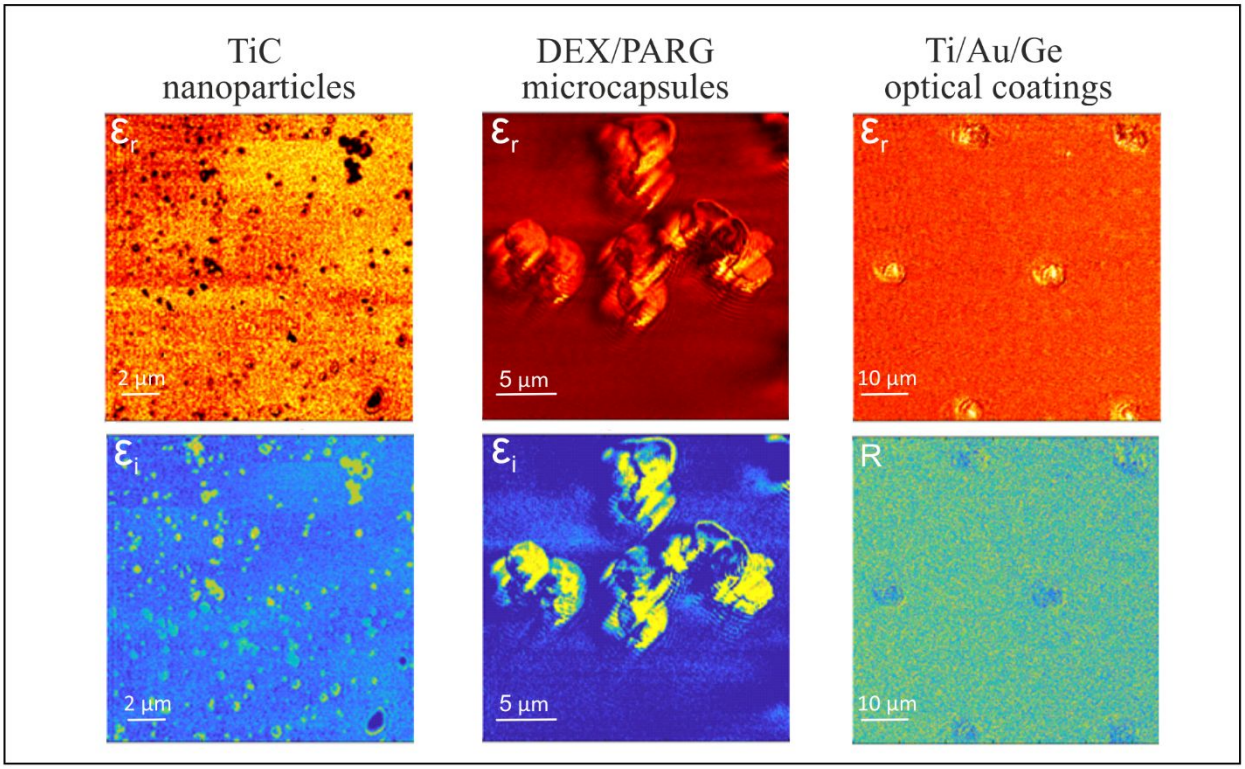

In this work we demonstrate the powerful capabilities of scattering-type Scanning Near-Field Optical Microscopy (s-SNOM) to map the complex permittivity of a specimen's surface at high-lateral resolution, in a set of precise applications focused on three distinct types of high-interest advanced nanostructured materials: (i) polyelectrolyte microcapsules for drug delivery assembled with layer-by-layer strategies, (ii) ultra-thin optical coatings with tunable color properties, and (ii) plasmonic ceramic nanoparticles.

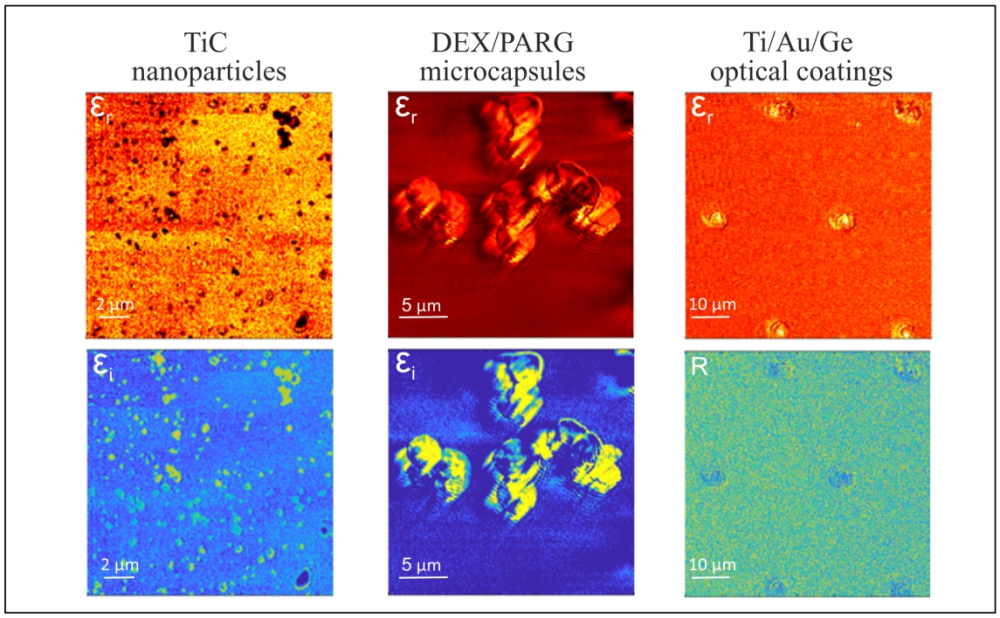

In this work we demonstrate the powerful capabilities of scattering-type Scanning Near-Field Optical Microscopy (s-SNOM) to map the complex permittivity of a specimen's surface at high-lateral resolution, in a set of precise applications focused on three distinct types of high-interest advanced nanostructured materials: (i) polyelectrolyte microcapsules for drug delivery assembled with layer-by-layer strategies, (ii) ultra-thin optical coatings with tunable color properties, and (ii) plasmonic ceramic nanoparticles.

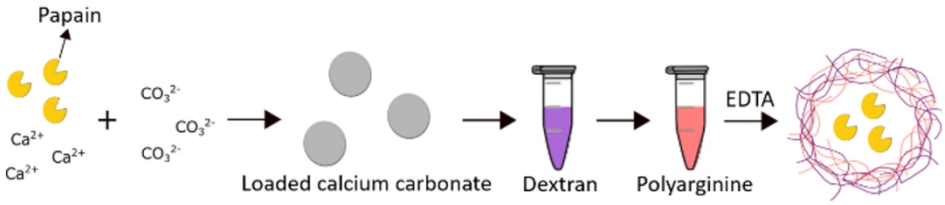

Figure 1 Process of fabrication of enzyme-loaded polyelectrolyte microcapsules.

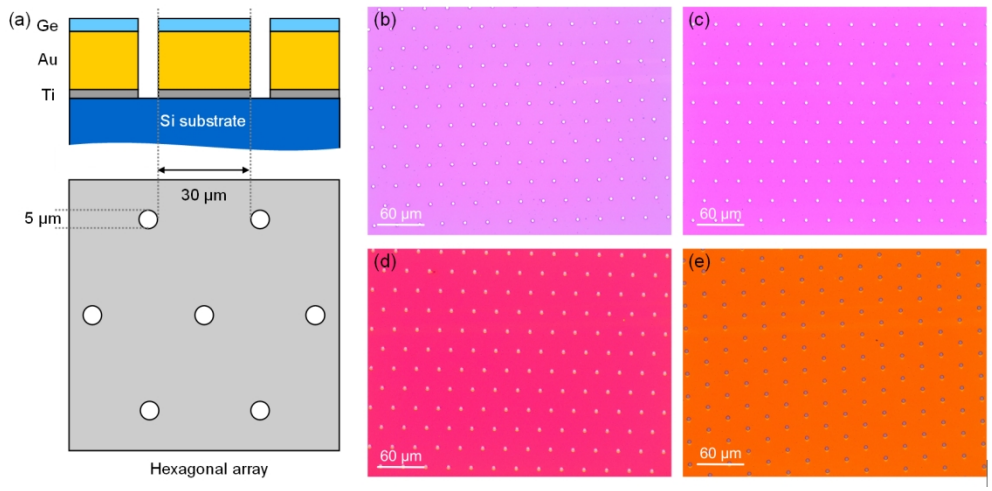

Figure 2 (a) Schematic illustrations of ultra-thin films with hole pattern array. (b-e) Brightfield microscope images of hole-patterned samples with different deposition angles (0, 30, 45, and 70°) at a thickness of 15 nm, respectively.

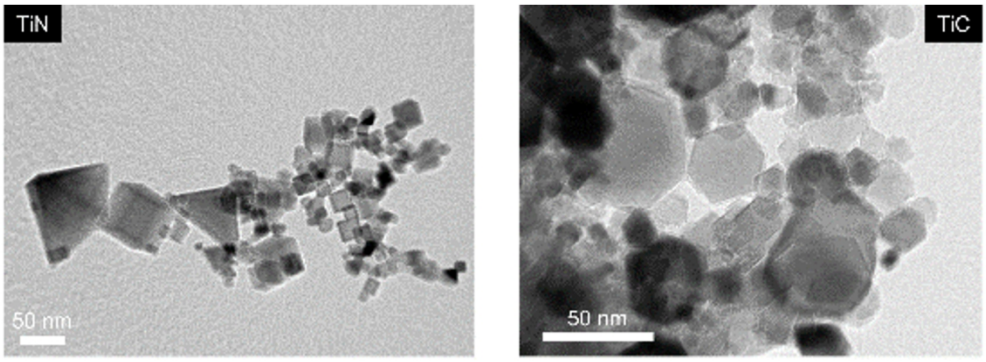

Figure 3 TEM Images of the investigated TiN (left) and TiC (right) NPs

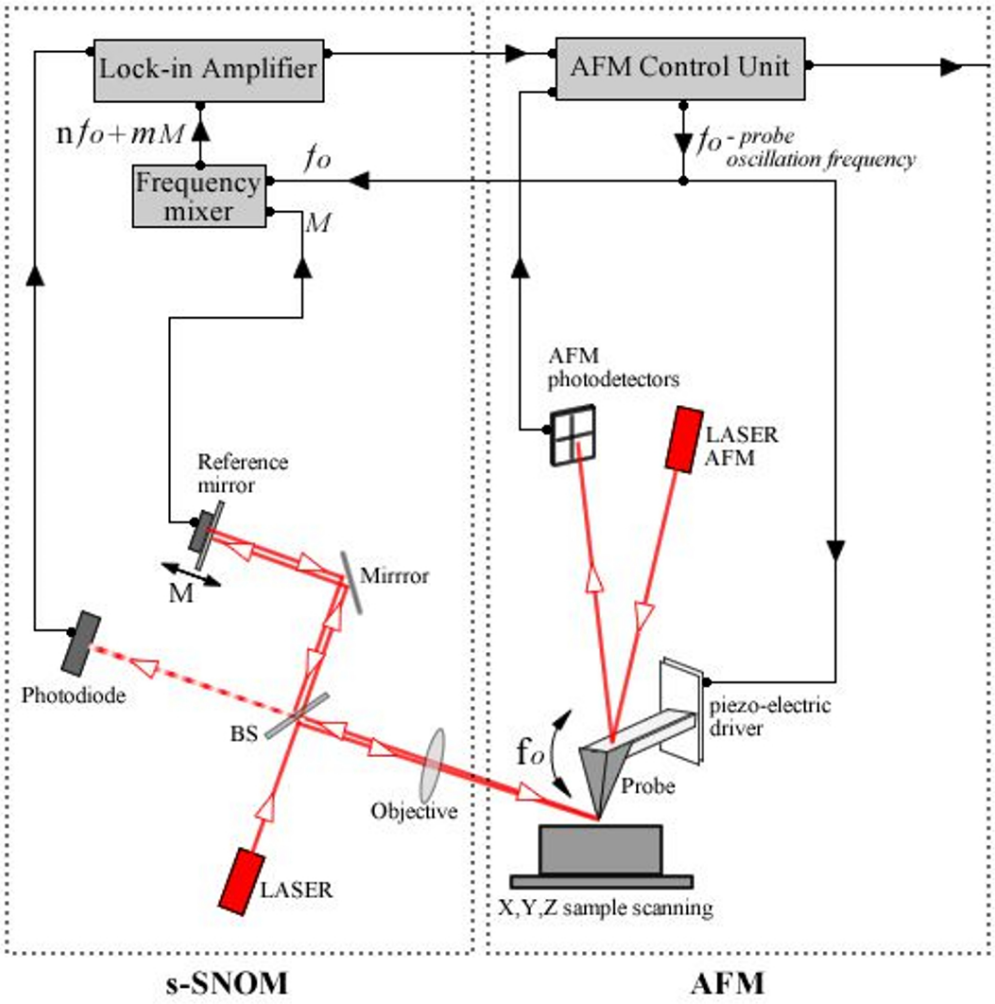

Figure 4. Home built s-SNOM experimental setup. (a) The s-SNOM setup is based on a pseudoheterodyne detection configuration, consisting in a modified Michelson interferometer with one interferometer arm focused onto the tip and the other one reflected off a harmonic oscillating reference mirror. The reference beam interferes with the scattered light originated from the near-field of the sample and the interference signal contains the near-field information at frequencies n·fo±m·M, where fo is the probe oscillation frequency, M is the mirror oscillation frequency and n, m are integers. The s-SNOM signal is collected using a lock-in amplifier locked at the n·fo±m·M spectral harmonics.

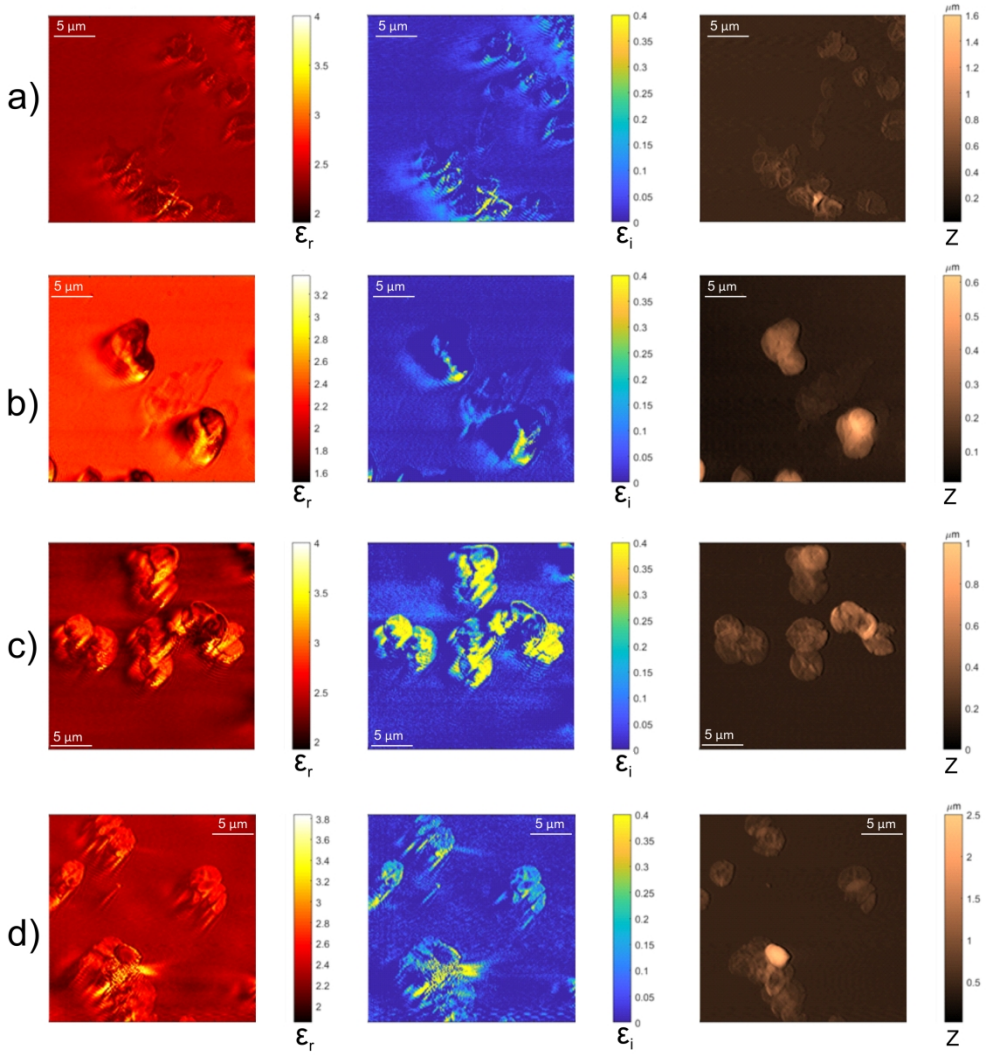

Figure 5. Complex permittivity and topography maps of dextran and polyarginine PMCs a) without entrapped enzymes, degraded by papain after b) 1h, c) 6h and d) 12h. Complex permittivity maps are calculated based on s-SNOM data, topography maps are collected with AFM.

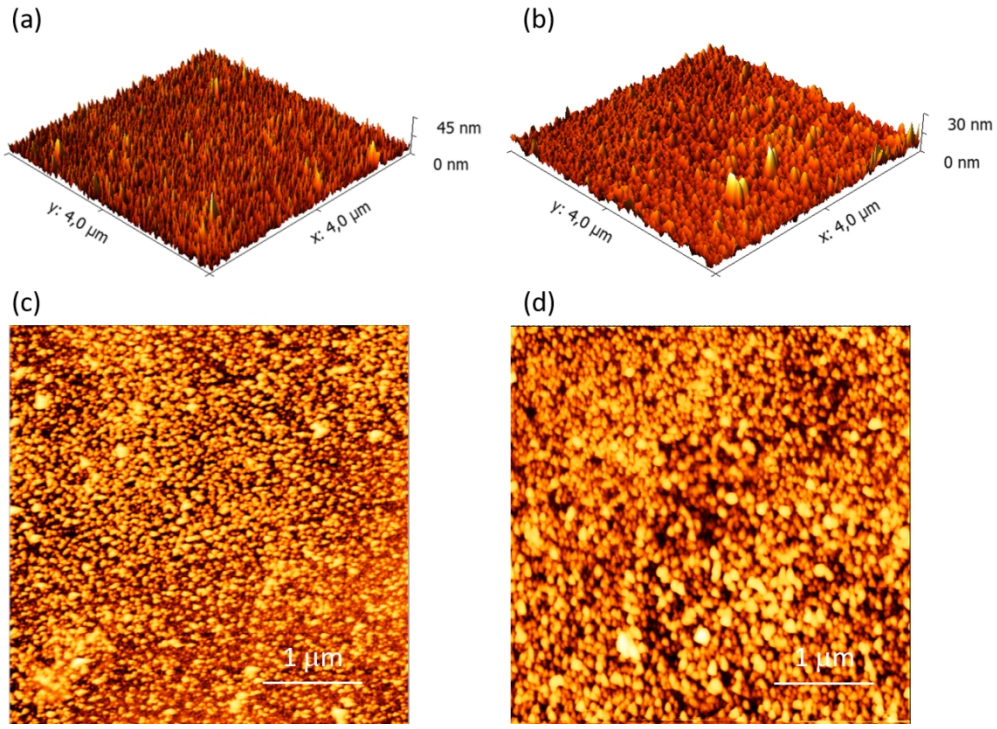

Figure 6. Topography of the DEX-PARG film: (a) and (c) topography of the pristine film; (b) and (d) report data after the immersion in ultrapure water.

343x251mm (96 x 96 DPI)

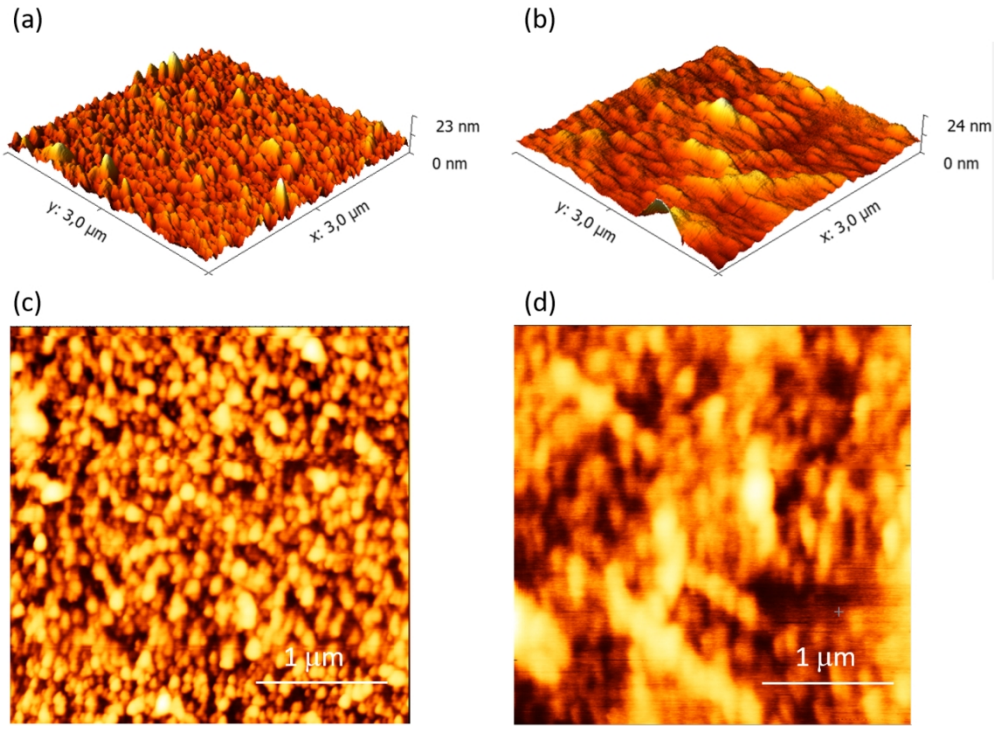

Figure 7 Topography of the DEX-PARG film. (a) and (c) refer to the film immersed in papain solution at room temperature, while (b) and (d) report data when the papain solution is kept at 37 °C.

343x252mm (96 x 96 DPI)

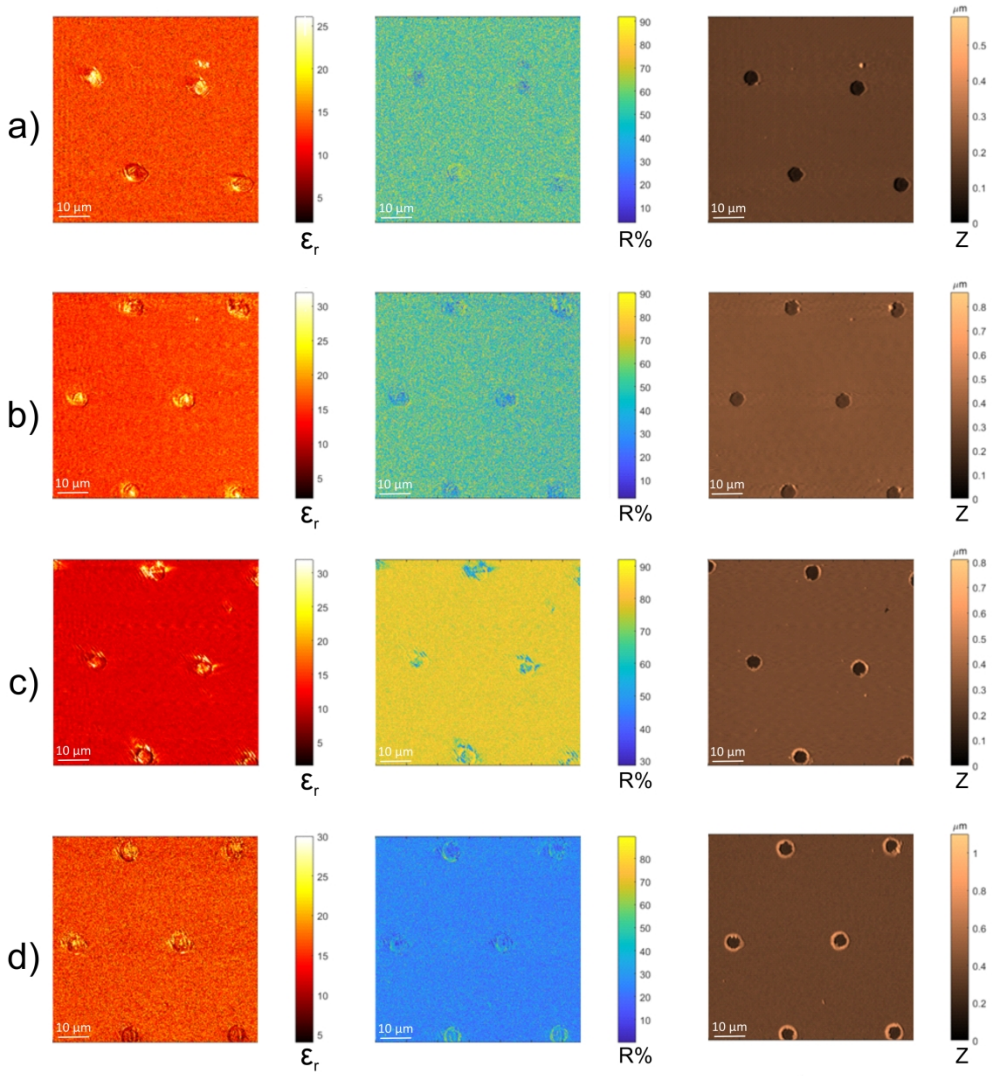

Fig. 8 Permittivity, reflectance and topography maps of Ti/Au/Ge UT-OCs. a) and b) depict samples with a 10 nm Ge layer deposited under a deposition angle of 0° and 70°, respectively. c) and d) depict samples with a 25 nm Ge layer deposited under a deposition angle of 0° and 70°, respectively. Permittivity and reflectance maps are calculated based on s-SNOM data; topography maps are collected with AFM.

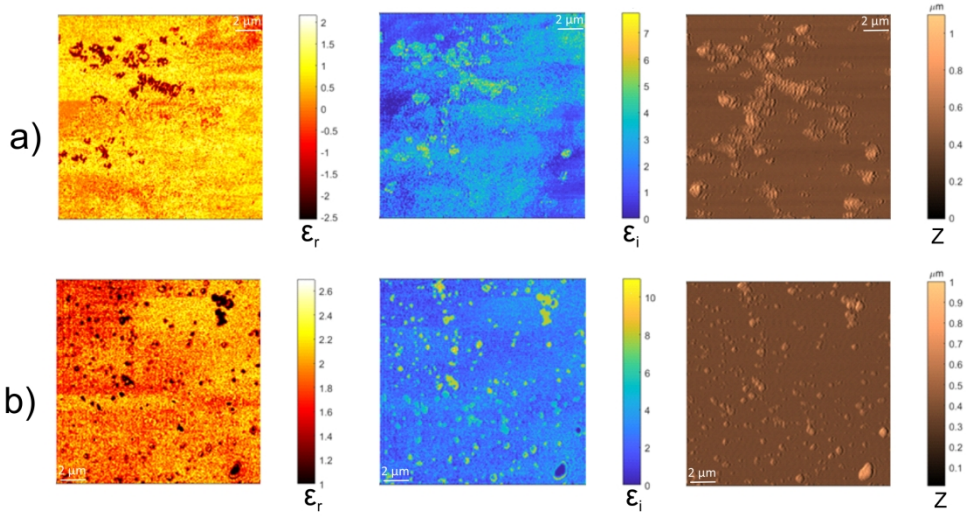

Fig. 9. Complex permittivity and topography maps of a) TiN and b) TiC NP clusters.

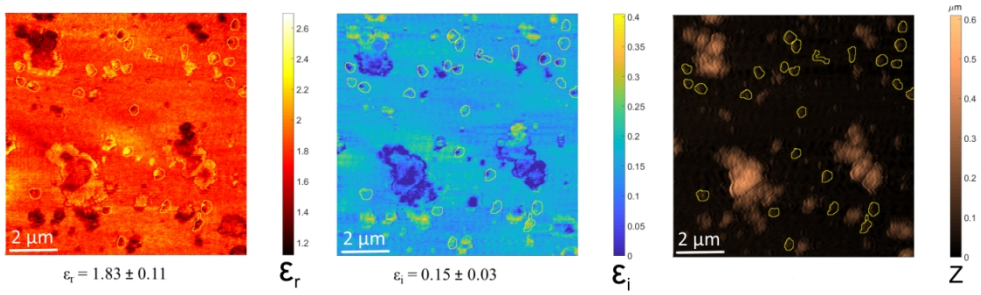

Fig. 10. Segmented topography and complex permittivity maps of TiC NP clusters in a 10x10 µm2 imaged area. Segmentations masks were computed on the AFM image for TiC formations with an area of particular size s, where 0.1 µm^2 <s < 0.2 µm^2 and were imposed on the complex permittivity maps derived from s-SNOM data. Mean εr/εi values are provided for the segmented TiC NP structures.

119x36mm (300 x 300 DPI)